# A Vertically Flow-Following Icosahedral Grid Model for Medium-Range and Seasonal Prediction. Part I: Model Description

RAINER BLECK,* JIAN-WEN BAO, STANLEY G. BENJAMIN, JOHN M. BROWN, MICHAEL FIORINO, THOMAS B. HENDERSON, JIN-LUEN LEE, ALEXANDER E. MACDONALD, PAUL MADDEN, JACQUES MIDDLECOFF, JAMES ROSINSKI, TANYA G. SMIRNOVA, SHAN SUN, AND NING WANG

*NOAA/Earth System Research Laboratory, Boulder, Colorado*

(Manuscript received 10 September 2014, in final form 4 February 2015)

ABSTRACT

A hydrostatic global weather prediction model based on an icosahedral horizontal grid and a hybrid terrain-following/isentropic vertical coordinate is described. The model is an extension to three spatial dimensions of a previously developed, icosahedral, shallow-water model featuring user-selectable horizontal resolution and employing indirect addressing techniques. The vertical grid is adaptive to maximize the portion of the atmosphere mapped into the isentropic coordinate subdomain. The model, best described as a stacked shallow-water model, is being tested extensively on real-time medium-range forecasts to ready it for possible inclusion in operational multimodel ensembles for medium-range to seasonal prediction.

## 1. Introduction

The invention of the fast Fourier transform (Cooley and Tukey 1965) has allowed spectral global circulation models to gain widespread acceptance in the last half century. However, the drawbacks of such models in terms of operations count and communications overhead at high spatial resolution have led, in recent years, to the development of gridpoint global models discretized on geodesic grids, commonly based on either the cube or the icosahedron (Tomita et al. 2001; Staniforth and Thuburn 2012). The main attraction of geodesic grids lies in their fairly uniform spatial resolution and in the absence of the two pole singularities found in spherical coordinates.

Icosahedral grids are generated by projecting an icosahedron onto its enclosing sphere and iteratively subdividing the 20 resulting spherical triangles until a desired spatial resolution is reached. For example, nine recursive bisections of triangle sides yield a mesh of roughly 2.6 million vertices spaced approximately 15 km apart.

While the term "finite volume" was not used at the time, early attempts to solve the barotropic vorticity equation on an icosahedral mesh (Williamson 1968; Sadourny et al. 1968) already embraced the finite-volume concept because Laplace and Jacobian operators had to be evaluated, for global conservation reasons, as line integrals along the perimeter of grid cells formed around each triangle vertex. The authors mentioned chose to define integration paths for the Laplace operator by what we today call Voronoi tessellation: the process of constructing grid cells by stringing together orthogonal bisectors of the triangle sides. The resulting "dual" mesh (dual to the triangular mesh) consists of mostly hexagons plus a dozen pentagons.

Experimentation with fluid models formulated on icosahedral grids resumed in the 1980s. Models built in the last three decades include, among others,

- a shallow-water model (SWM) in vorticity–divergence form (Masuda and Ohnishi 1987);
- an SWM in vorticity–divergence form (Heikes and Randall 1995a);
- a three-dimensional extension of the above, offering a choice of vertical coordinates (Randall et al. 2000; Ringler et al. 2000);

* Current affiliation: NASA Goddard Institute for Space Studies, New York, New York.

*Corresponding author address:* Rainer Bleck, NOAA/Earth System Research Laboratory, Global Systems Division, 325 Broadway, Boulder, CO 80305.
E-mail: rainer.bleck@noaa.gov

DOI: 10.1175/MWR-D-14-00300.1

- an SWM using potential vorticity as the prognostic variable (Thuburn 1997);
- the operational global weather prediction model of the German Weather Service (Majewski et al. 2002);
- a nonhydrostatic general circulation model on a mesh fine enough for cloud-permitting simulations (Tomita et al. 2004; Satoh et al. 2008);
- a nonhydrostatic model permitting clustering of grid points in one particular region of the globe (Ringler et al. 2011; Skamarock et al. 2012); and
- a nonhydrostatic model (Gassmann 2013; Zängl et al. 2015) designed to be a unified tool for both weather prediction and climate simulation.

Some of these models solve the momentum equations while others solve the vorticity and divergence equations. A common feature (virtually obligatory in unstructured-grid models) is the use of finite-volume numerics on the dual pentagonal/hexagonal grid. The three-dimensional models in the above list, with the exception of the isentropic coordinate model described by Randall et al. (2000), use various combinations of terrain-following and isobaric vertical coordinates. A hybrid-isentropic coordinate version of the Ringler et al. (2000) model is referenced in Lauritzen et al. (2010), and an isentropic upper atmosphere extension of the Thuburn (1997) model is referenced in Pulido and Thuburn (2006).

This article describes a model—named the Flow-Following Icosahedral Model (FIM)—that has been developed at the Earth System Research Laboratory of the U.S. National Oceanic and Atmospheric Administration. The groundwork for FIM was laid in an SWM developed by Lee and MacDonald (2009), Lee et al. (2010), and MacDonald et al. (2011). Some aspects of the expansion of the SWM into a full-fledged medium-range weather prediction tool are described in Bleck et al. (2010). The upgrade from two to three spatial dimensions brought with it the attribute "flow following" to characterize FIM's predominantly Lagrangian vertical coordinate.

Specifically, FIM is a "stacked shallow-water model" in which vertical resolution is provided by a combination of quasi-Lagrangian isentropic layers in the free atmosphere and terrain-following ($\sigma$ coordinate) layers near the ground. With its adaptive, arbitrary Lagrangian–Eulerian (ALE; Hirt et al. 1974)-like attributes, this vertical coordinate is similar to a coordinate used successfully in weather and ocean models such as the Rapid Update Cycle (RUC; Bleck and Benjamin 1993; Benjamin et al. 2004) and Hybrid Coordinate Ocean Model (HYCOM; Bleck 2002).

The primary purpose of using a near-isentropic vertical coordinate in a circulation model is to assure that momentum and mass field constituents (potential temperature, moisture, chemical compounds, etc.) are dispersed in the model in a manner emulating reality, namely, along neutrally buoyant surfaces.

Lateral dispersion occurs in a model not only because of the action of explicit horizontal eddy mixing terms but also because of truncation errors arising during lateral transport. By confining both types of dispersion to neutrally buoyant surfaces, isentropic modeling offers a path toward reducing the cold bias in conventional general circulation models that Johnson (1997) has shown to be a consequence of entropy generation by nonphysical, diabatic lateral mixing. There is considerable evidence by now (Zhu and Schneider 1997; Webster et al. 1999; Schaack et al. 2004; Chen and Rasch 2012) that isentropic coordinate models are in fact capable of reducing this bias.

Numerically induced vertical dispersion likewise is reduced if layer interfaces act like material surfaces, as isentropic surfaces do on short time scales, during the passage of internal gravity waves. Figure 9 in Benjamin et al. (2004) demonstrates the overall reduction of interlayer transport velocity (and, by implication, its dispersive effects) achievable in an isentropic coordinate model.

Physical parameterizations in FIM match those used operationally by the Global Spectral Model in the Global Forecast System (GFS) of the National Centers for Environmental Prediction (NCEP). FIM is being validated on the basis of extended-range, real data forecasts using GFS initial conditions.

We split the description of FIM into two parts. Part I (this article) describes the dynamic equations and the numerical algorithms used to solve them, as well as results from an idealized model test. Part II will primarily deal with real data applications.

## 2. Basic equations

Following tradition, we express the model equations in a local coordinate system $(x, y, s)$, where $x, y$ measure distances along Earth's surface, and $s$ is an arbitrary but monotonic function of height, subject only to the requirement that the bottom and top of the model atmosphere are $s$ surfaces. The physical dimensions of $s$ are arbitrary; in fact, $s$ can be chosen to be a continuous extension of the layer index.

An important point to note is that, regardless of the definition of $s$, coordinate surfaces $x$ = const and $y$ = const continue to be vertical surfaces. This implies that the horizontal velocity vector $\mathbf{v} = (\dot{x}, \dot{y})$ measures speed along a geopotential surface and that the intersections of $x$, $y$ surfaces, marking the direction in which the hydrostatic equation is solved, continue to point in the direction of gravity.

Stated differently, the momentum equation solved in generalized vertical coordinate models retains the

component form it would have in $x$, $y$, $z$ coordinate models. The decomposition into Cartesian vector components is essential for separating the gravitational force from the much weaker inertial forces. The $s$ coordinate only enters when it comes to deducing the horizontal pressure gradient from data residing on $s$ surfaces.

Let $\nabla_s$ be the 2D gradient operator at $s$ = const; $\Pi = c_p(p/p_0)^{R/c_p}$ the Exner function; $T$ the virtual temperature; $\theta = c_p T/\Pi$ the potential virtual temperature; $\phi = gz$ the geopotential; $M = \phi + \Pi\theta$ the Montgomery potential; $\zeta$ the relative vorticity (i.e., the vertical or $\mathbf{k}$ component of the velocity curl vector); $\dot{\theta}$ the net diabatic heating rate; and $\mathbf{F}$ the sum of frictional forces. The set of dynamic equations solved in FIM can then be formulated as follows [see Kasahara (1974) and Bleck (1978) for detailed derivations]:

*Mass conservation*:

$$\frac{\partial}{\partial t}\left(\frac{\partial p}{\partial s}\right) + \nabla_s \cdot \left(\mathbf{v}\frac{\partial p}{\partial s}\right) + \frac{\partial}{\partial s}\left(\dot{s}\frac{\partial p}{\partial s}\right) = 0, \tag{1}$$

*Thermal energy conservation*:

$$\frac{\partial}{\partial t}\left(\theta\frac{\partial p}{\partial s}\right) + \nabla_s \cdot \left(\mathbf{v}\frac{\partial p}{\partial s}\theta\right) + \frac{\partial}{\partial s}\left(\dot{s}\frac{\partial p}{\partial s}\theta\right) = \dot{\theta}\frac{\partial p}{\partial s}, \tag{2}$$

*Momentum conservation*:

$$\frac{\partial \mathbf{v}}{\partial t} + (\zeta + f)\mathbf{k}\times\mathbf{v} + \left(\dot{s}\frac{\partial p}{\partial s}\right)\frac{\partial \mathbf{v}}{\partial p} + \nabla_s\left(M + \frac{\mathbf{v}^2}{2}\right) - \Pi\nabla_s\theta = \mathbf{F}, \quad \text{and} \tag{3}$$

*Hydrostatic equation*:

$$\frac{\partial M}{\partial \theta} = \Pi. \tag{4}$$

Conservation equations for mass field constituents (tracers for short), such as gaseous, liquid, frozen water, and chemical compounds, have the same form as (2). Source and sink terms in these equations—the analogs of $\dot{\theta}\partial p/\partial s$—are governed by additional equations expressing what is commonly called "model physics."

The term $\mathbf{F}$ in (3) comprises surface drag and various kinetic energy dissipation processes, such as stirring by subgrid-scale motion. It is important to note that explicit lateral mixing is not needed in FIM for numerical stability reasons. The dissipative properties of the horizontal numerical discretization scheme (see below) appear to be sufficient to counteract accumulation of energy on the grid scale. Nevertheless, slight explicit lateral mixing has been found to improve forecast accuracy.

Vertical turbulent mixing of $\theta$, tracers, and momentum is accounted for in model physics; it affects resolved-scale model fields via the term $\dot{\theta}$ on the right-hand side of (2) and the forcing term $\mathbf{F}$ in (3).

Discretization in the vertical is accomplished in FIM by integrating prognostic variables, as well as their governing equations, over individual layers bounded by $s$ surfaces. FIM actually goes one step further. Following the shallow-water paradigm, it views the atmospheric state as one in which most variables are piecewise constant in the vertical with discontinuities across $s$ surfaces.

Introducing the stairstep discretization of $\theta$ in the hydrostatic equation [(4)] implies that $M$ is vertically constant in each coordinate layer. Since $\nabla_s\theta$ is vertically constant by definition as well, the pressure force terms in (3), if formulated with a midlayer value for $\Pi$, do not create vertical shear within a coordinate layer. Thus, there is no need to distinguish $\mathbf{v}$ from its layer average $\overline{\mathbf{v}}$. The layer-averaged momentum conservation equation [(3)] can therefore be written as

$$\frac{\partial \mathbf{v}}{\partial t} + (\zeta + f)\mathbf{k}\times\mathbf{v} + \frac{1}{\Delta p}\left[\left(\dot{s}\frac{\partial p}{\partial s}\right)_2(\hat{\mathbf{v}}_2 - \mathbf{v}) - \left(\dot{s}\frac{\partial p}{\partial s}\right)_1(\hat{\mathbf{v}}_1 - \mathbf{v})\right] + \nabla_s\left(M + \frac{\mathbf{v}^2}{2}\right) - \overline{\Pi}\nabla_s\theta = \mathbf{F}. \tag{5}$$

Here, indices 1 and 2 denote the upper and lower interface, respectively, of the layer in question, and $\Delta p = p_2 - p_1$. The vertical advection terms, that is, those involving $\dot{s}$, have been arrived at by integrating

$$\frac{1}{\Delta p}\int\left(\dot{s}\frac{\partial p}{\partial s}\right)\frac{\partial \mathbf{v}}{\partial p}\,dp$$

by parts. They involve velocity values on interfaces, denoted here by $\hat{\mathbf{v}}$. Since $\mathbf{v}$ is allowed to be discontinuous at interfaces, the definition of $\hat{\mathbf{v}}$ is to some extent arbitrary and in practice depends on the choice of vertical advection scheme.

The layer-integrated mass and thermal energy conservation equations [(1), (2)] assume the forms

$$\frac{\partial \Delta p}{\partial t} + \nabla_s \cdot (\mathbf{v}\Delta p) + \left(\dot{s}\frac{\partial p}{\partial s}\right)_2 - \left(\dot{s}\frac{\partial p}{\partial s}\right)_1 = 0, \quad \text{and} \tag{6}$$

$$\frac{\partial(\theta\Delta p)}{\partial t} + \nabla_s \cdot (\theta\mathbf{v}\Delta p) + \left(\dot{s}\frac{\partial p}{\partial s}\hat{\theta}\right)_2 - \left(\dot{s}\frac{\partial p}{\partial s}\hat{\theta}\right)_1 = \overline{\dot{\theta}}\Delta p. \tag{7}$$

As in (5), the caret denotes interface values needed in the vertical transport terms. The method by which they are constructed (upstream, centered, ...)

determines properties such as monotonicity and diffusiveness of vertical advection in the model. Equations for other mass field tracers (moisture, etc.) have the same form as (7).

Regardless of whether $\theta$ represents potential temperature or another mass field tracer, it is generally necessary to retrieve its value (which represents tracer mixing ratio) from the product $\theta\Delta p$ representing the amount of $\theta$ per unit area in the given layer. This operation becomes ill-conditioned if $\Delta p$ at the end of a time step is much smaller, by one or more orders of magnitude, than at the beginning. In FIM, we avoid generating spurious values when dividing $\Delta p$ into $\theta\Delta p$ by requiring that the new $\theta$ value remain within the range spanned by the old $\theta$ values at the grid point in question and its neighbors.

Unfortunately, this introduces an element of nonconservation into the transport process for which a number of ''engineering'' remedies are available, such as distributing the $\theta$ amount gained or lost among neighboring grid cells. Since this problem only arises during the rare occasions when a cell exports most (but not all) of its mass during a single time step, the $\theta$ amount in question tends to be small and redistributing it is generally not worth the computational effort.

## 3. The dynamic core

### a. Time differencing

Given right-hand side values for the generic differential equation $u_t = F(u, x, t)$ at three consecutive time levels $n-2$, $n-1$, $n$, and $u$ at time level $n$, the third-order Adams–Bashforth scheme (Durran 1991) expresses $u$ at time level $n+1$ as

$$u^{n+1} = u^n + \frac{\Delta t}{12}(23F^n - 16F^{n-1} + 5F^{n-2}), \qquad (8)$$

where $\Delta t$ is the model time step. The Adams–Bashforth scheme is an explicit scheme and requires only one evaluation of $F$ per time step. Previous studies (MacDonald et al. 2000) have shown that it is an accurate and efficient scheme for numerical weather prediction models.

### b. The icosahedral horizontal mesh

The icosahedron has 20 equilateral triangular faces. When each triangle side is replaced by a geodesic curve on the enclosing sphere, we obtain a perfect spherical mesh. However, as we recursively subdivide the triangles and project the newly formed vertices onto the sphere, most of the resulting spherical subtriangles lose their regularity and uniform size. Additional steps are usually taken to reduce the degree of imperfection.

Two criteria measure the numerical quality of an icosahedral grid on the sphere. One is its uniformity, which affects the maximum time step allowed for solving the prognostic equations; the other is the regularity of its dual Voronoi cell mesh, which affects the accuracy of numerical solutions (Heikes and Randall 1995b; Tomita et al. 2001; Du et al. 2003; Peixoto and Barros 2013). It appears that one cannot optimize both simultaneously. The present FIM grid is based on a modified recursive generation algorithm described in Wang and Lee (2011). This algorithm produces icosahedral grids with better uniformity and regularity compared to grids based on the standard recursive construction method of Baumgardner and Frederickson (1985).

An important point to note is that the governing equations in FIM are not solved in spherical coordinates but in stereographic projections of each icosahedral grid cell onto its local tangent plane (Lee and MacDonald 2009).

### c. Horizontal finite-volume operators

Owing to its heritage (Lee and MacDonald 2009), variables in FIM are horizontally unstaggered. The governing equations are solved using finite-volume techniques (van Leer 1977; Lin et al. 1994) that define model variables as mean quantities over each grid cell. As already mentioned, the need to build conservation laws for various quantities into the finite-difference equations on unstructured grids (the icosahedral grid, despite its regularity, is ''unstructured'' in this context) requires that grid-cell averages of vorticity, divergence, and gradient be expressed by line integrals along the grid cell perimeter:

$$\zeta = A^{-1}\oint \mathbf{v}\cdot d\mathbf{s}; \quad \nabla\cdot\mathbf{v} = A^{-1}\oint \mathbf{v}\cdot d\mathbf{n};$$
$$\nabla p = A^{-1}\oint p\, d\mathbf{n}. \qquad (9)$$

Here, $d\mathbf{s}$ is an infinitesimal vector increment along the horizontal curve circumscribing the grid cell of area $A$, and $d\mathbf{n} = d\mathbf{s}\times\mathbf{k}$, where $\mathbf{k}$ is the vertical unit vector. The hexagonally and pentagonally shaped elements of the icosahedral mesh are well suited for approximating such line integrals.

The recipe for evaluating the line integrals [(9)] in FIM is to sum up integrals taken along the five or six individual edge segments, each one approximated by the trapezoidal rule. The required vertex values of the integrand are computed as unweighted averages of their

respective three surrounding cell values. (Preserving second-order accuracy of this interpolation scheme in the case of distorted grid cells requires nonuniform averaging weights. Such a scheme has been developed but is not used at this time.)

As mentioned, adding explicit lateral mixing terms to some or all prognostic equations is not required for maintaining numerical stability but may still be advisable to suppress computational modes that occasionally make their presence known on FIM's horizontally unstaggered grid. We presently rely on weak biharmonic lateral momentum mixing to dampen these modes. Specifically, the stress term $\mathbf{F}$ in (5), which originally encompassed surface friction, turbulent vertical mixing, and Rayleigh damping of gravity waves near the model top, now also includes the term

$$\frac{1}{\Delta p}\nabla\cdot[\nu\Delta p\nabla(-A\nabla^2\mathbf{v})],$$

where $\nu$ is an eddy viscosity. We presently hold $\nu$ constant except for a ramp-up in the uppermost coordinate layers to reduce gravity wave reflection at the model top. The negative Laplacian $-A\nabla^2 f$ ($f$ being an arbitrary scalar) is evaluated by subtracting from each gridpoint value $f$ the average of its five or six surrounding neighbors. This interpretation of the Laplace operator is based on Gauss's theorem applied to the integral of $\nabla^2 f$ over grid cell area $A$:

$$\iint_A(\nabla^2 f)\,dA=\iint_A\nabla\cdot(\nabla f)\,dA=\oint(\nabla f)\cdot d\mathbf{n}.$$

Numerically approximating the gradient of $f$ normal to the grid cell perimeter and integrating along the perimeter leads to the above-mentioned expression for the Laplacian.

Global constraints like mass conservation, zero net pressure force, and zero net circulation require exact cancellation of integral segments evaluated in the two cells bordering a given edge segment. In FIM, which solves equations on local stereographic projections (Lee and MacDonald 2009), exact mass conservation is easily achieved by evaluating mass fluxes on projection planes centered on cell edges, but the two other constraints mentioned cannot be satisfied exactly.

The root of the problem is the requirement that the edge vectors $d\mathbf{s}$ in (9) form a polygon—otherwise the gradient of a constant field would not be zero. This can only be achieved by representing the vectors circumscribing a given grid cell on a projection plane centered on this cell. Even if tangential velocity components needed for computing vorticity are represented on edge-centered projection planes, which render them equal and opposite when viewed from the two adjoining cells, the product $(\mathbf{v}\cdot d\mathbf{s})$ does not cancel because the increments $d\mathbf{s}$ are defined on two different stereographic maps.

Line integrals yielding pressure gradients, likewise, must use edge vectors expressed in a cell-centered coordinate system, which again precludes exact global cancellation. The error involved is small but nevertheless may lead to biases in the model climatology. To ready FIM for a possible future role as a component in an Earth system model, we therefore intend to move line integrations from local stereographic projections back to the sphere.

[Additional constraints, such as the requirement that there be no barotropic spinup over a flat bottom, may not be achievable on the unstructured icosahedral mesh. This particular constraint must be applied to the numerical rendition of the pressure torque (Arakawa and Lamb 1977) that, being a line integral of a line integral, cannot be manipulated as easily as conventional finite-difference expressions on a logically rectangular grid.]

Accurate evaluation of the horizontal pressure gradient force (PGF) in the momentum equation is known to be numerically challenging on steeply inclined coordinate surfaces where the term $\rho^{-1}\nabla_z p$ becomes the residual of two large opposing contributions, $\rho^{-1}\nabla_s p$ and $\nabla_s\phi$. This is not an issue in FIM's $\theta$-coordinate subdomain because the PGF expression shown in (5), $\nabla_s M-\Pi\nabla_s\theta$, reduces to $\nabla_s M$ as $s\to\theta$. To retain the advantage of a single-term PGF expression in the $\sigma$-coordinate subdomain where $\nabla_s\theta$ can be large, we optionally use in the lower part of the model domain a scheme proposed by Janjic (1977) that expresses the PGF as $\nabla_p\phi$ and finds $\phi$ at neighboring grid points by performing additional hydrostatic integrations to the appropriate pressure level.

Terrain height is derived from a dataset of 10-km resolution that in turn is based on the 30-s GTOPO30 dataset. Interpolation to the FIM grid is via unweighted averaging of data points falling within a circle of radius $1.25\times$ mesh size.

### d. *Flux-corrected transport*

The term layer model describes a class of models in which the vertical spacing of layer interfaces is variable in space and time, with interface movement controlled primarily by the convergence and divergence of horizontal mass fluxes within each layer. FIM belongs to this class of vertically quasi-Lagrangian models. To assure the numerical integrity of a layer model, mass fluxes must be constructed with strong emphasis on positive definiteness and monotonicity of the layer thickness field. The scheme chosen for this purpose in FIM is known as flux-corrected transport (FCT; Boris and

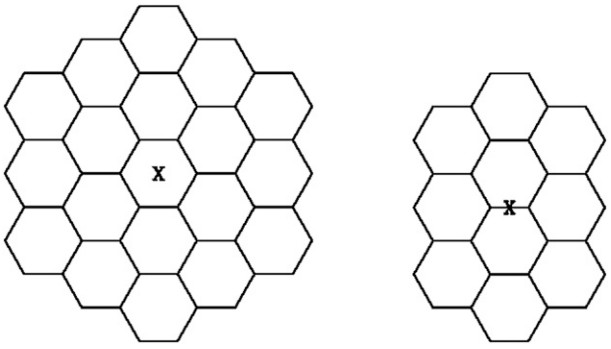

FIG. 1. (left) Stencil of grid cells affecting the outcome of thickness change calculations in the central cell marked by X. (right) Stencil of grid cells affecting the calculation of mass fluxes across the central hexagonal edge segment marked by X. Note that these are composite stencils; individual passes through the grid involve interactions with nearest neighbors only.

Book 1973; Zalesak 1979). The multistep operation is numerically complex and results in a fairly large horizontal stencil, as illustrated in Fig. 1 for the case of a hexagonal grid and space-centered flux expressions of second-order accuracy.

Given a transport equation of the type $u_t = -F_x$, where $F$ represents the flux of the variable $u$ in $x$ direction, the FCT scheme proceeds in two steps. In step 1, the $u$ field is advanced in time using an upstream, forward-in-time (low order) scheme for computing $F_x$ that because of its diffusive character is known to maintain positive definiteness and monotonicity. In step 2, antidiffusive fluxes based on more accurate (high order) approximations are added to the diffusive fluxes. In what constitutes the essence of FCT, these antidiffusive fluxes are locally reduced or "limited" just enough to avoid violating the positive definiteness constraint and creating new extrema in $u$.

In contrast to the usual practice of forming high-order fluxes from space-centered fourth- or sixth-order finite-difference expressions, high-order fluxes are constructed in FIM in the spirit of the (at best) second-order piecewise linear method (PLM) scheme (van Leer 1974; Colella and Woodward 1984). In one spatial dimension, PLM is monotonicity preserving. It may be possible, with some effort, to preserve this property even in the present case where each cell exchanges mass with five or six neighbors. We have not yet explored this possibility, relying instead on FCT-type flux limiting. The spatial average of the transported variable in the slab upstream of a cell edge is computed by assuming that the variable changes linearly between neighboring cell centers.

To adapt the low-order transport scheme and the flux-limiting algorithm, both of which are inherently two time level schemes, to the four time level scheme [(8)], we proceed as follows:

1) Low-order fluxes from three consecutive time levels are combined as shown in (8) to generate a low-order solution at time level $n + 1$.
2) The flux-limiting process is based on "worst-case" tendencies of the transported variable, obtained by selectively bundling high-order incoming and outgoing fluxes. These tendencies are computed in FIM by combining, in the manner of the right-hand side of (8), the current unclipped high-order flux $F^n$ with the "final," that is, low-order plus clipped antidiffusive, fluxes from the previous two time levels: $F^{n-1}$, $F^{n-2}$.
3) The clipped antidiffusive fluxes are combined with the low-order ones to form final fluxes $F^n$; these are then used in (8) to compute the final value of $u^{n+1}$.

Horizontal transports of $\theta$ and tracers are handled analogously. The prototype transport term for these variables is $\nabla \cdot (\theta \mathbf{v} \Delta p)$ in (7). Antidiffusive fluxes are limited in this case on the basis of extrema in the transported variable $\theta$ itself, not extrema in the product $\theta \Delta p$. This is to say that we enforce monotonicity in the tracer mixing ratio field, not in the tracer amount.

Potentially more accurate transport schemes, such as the one by Dubey et al. (2014), are under consideration for future use. However, the trade-off between accuracy and computational effort remains an issue.

### e. *Vertical mesh*

As already mentioned, FIM is a layer or stacked shallow-water model, meaning that the thickness of individual coordinate layers—in other words, the spacing of grid points in the vertical—can change in space and time. Hence, FIM output contains an extra three-dimensional field, layer thickness, not found in traditional three-dimensional circulation models.

Layer thickness is not a "new" prognostic variable requiring an additional prognostic equation. Hydrostatic models in general solve the shallow-water form of the continuity equation to determine material vertical motion. They then split this motion up in various ways into motion of the coordinate surface and motion relative to the coordinate surface. The split is particularly trivial in the two limiting cases of a material vertical coordinate and a fixed vertical grid where 100% of the material motion is assigned to one or the other term, respectively. In FIM, the splitting algorithm is more elaborate because grid points in the isentropic subdomain follow the air motion (in the absence of diabatic heating or cooling, that is), while grid points in the lower part of the atmosphere are placed according to the rules for terrain-following coordinates.

We refer to the algorithm regulating vertical spacing of grid points as the grid generator. It continually restores layers to their assigned "target" $\theta$ values, while at the same time keeping an eye on minimum thickness constraints.

The grid generator is described in detail in sections 4 and 5 of Bleck et al. (2010). As presently formulated, it does not enforce a minimum layer thickness constraint in the isentropic domain. A special scheme that diffuses mass among layers and thereby reduces layer-to-layer thickness contrasts, but does so without changing $\theta$ in the participating layers, is used to prevent layer collapse in the isentropic subdomain. The scheme is based on one developed for oceanic use by McDougall and Dewar (1998).

### f. Long time step tracer transport

The use of the numerically complex FCT scheme makes lateral transport costly in FIM. If the model were to be used to simulate the evolution of $O(100)$ interacting chemical species, execution time would be prohibitive. One approach to reducing the amount of time spent in the FCT routine is to carry out tracer transport intermittently, using a longer time step. This split approach is possible because the time step in FIM dynamics is controlled by the speed of gravity and Lamb waves, not by the typically much smaller wind speed that governs transport processes. In other words, advecting tracers using a time step geared toward maintaining numerical stability in gravity wave transmission is not very cost-effective.

Because of the fluctuating height of grid cells, tracer conservation during long time step transport is not easily achieved in layer models if vertical mass fluxes are involved. [Lin (2004) describes a scheme for the simpler case of a vertically Lagrangian mesh.] Since the transport equations in layer models are formulated in flux form, transport with a time step longer than $\Delta t$, say, $J\Delta t$, where $J > 1$, must be based (Sun and Bleck 2006) on a rigorously time-integrated form of the mass continuity function (6):

$$\frac{\Delta p^{n+J} - \Delta p^{n}}{J\Delta t} + \nabla_s \cdot \overline{\mathbf{v}\Delta p}^{J} + \left(\overline{\dot{s}\frac{\partial p}{\partial s}}^{J}\right)_2 - \left(\overline{\dot{s}\frac{\partial p}{\partial s}}^{J}\right)_1 = 0, \tag{10}$$

where the overbar denotes integration over $J$ time steps. To assure that the equation is exactly satisfied in the model, the layer thickness and velocity fields in FIM must already have been stepped forward from time level $n$ to $n + J$. At that instant, both the tendency term and the horizontal flux divergence term [terms 1 and 2 in (10)] can be determined; the latter can be done by summing up the instantaneous fluxes over the past $J$ time steps. The time-integrated vertical flux terms (terms 3 and 4) can then be obtained by vertically summing up (10), using $\dot{s} = 0$ at the top or bottom of the column as a starting point.

By combining (10) with the equation $dQ/dt = 0$, expressing conservation of a tracer $Q$ during transport (sources and sinks of $Q$ can be evaluated separately), we arrive at the transport equation

$$\frac{(Q\Delta p)^{n+J} - (Q\Delta p)^{n}}{J\Delta t} + \nabla_s \cdot (Q\overline{\mathbf{v}\Delta p}^{J}) + \left(\overline{\dot{s}\frac{\partial p}{\partial s}}^{J}\hat{Q}\right)_2 - \left(\overline{\dot{s}\frac{\partial p}{\partial s}}^{J}\hat{Q}\right)_1 = 0, \tag{11}$$

which can be solved for the tracer amount $Q\Delta p$ at time level $n + J$. The meaning of the caret and the method by which $Q\Delta p$ is converted to the tracer mixing ratio $Q$ were discussed in the context of (7).

Equation (11) is solved by flux-corrected transport. Details are as follows:

1) Vertical $Q$ fluxes are based on the piecewise parabolic method (PPM; Colella and Woodward 1984). To avoid numerical stability problems posed by combinations of large vertical velocities and thin layers, integration of $Q$ over the slab upstream of a given interface must be allowed to extend over multiple layers.
2) The vertical PPM-based fluxes are used in conjunction with horizontal upstream fluxes to arrive at a low-order solution for $Q$.
3) High-order horizontal fluxes are of second-order accuracy; that is, they involve averages of $Q$ over two neighboring grid cells.
4) The limiters applied to the antidiffusive (high minus low order) fluxes to assure monotonicity are based on the maxima and minima of "old" $Q$ values in (i) the cell in question, (ii) its lateral neighbors, and (iii) the upstream slab(s) above or below the cell.

Comparisons of tracer fields advected over long and short time steps indicate that $J = 10$ works well in general, the single exception encountered so far being late winter major stratospheric warming events when winds in the meso- and upper stratosphere can reach speeds $> 150\ \mathrm{m\,s^{-1}}$. In those few cases, $J$ had to be reduced to 5 to yield meaningful results.

Note that (6) is solved using the three time level Adams–Bashforth time differencing scheme, whereas transport in (11) is carried out in forward-in-time mode. To achieve consistency between the thickness tendency term and the horizontal mass flux divergence, mass

fluxes from three consecutive time levels must therefore be combined in the manner indicated in (8) before they are added to the flux time integral.

While three-dimensional transport is the dominant process by which tracers are redistributed in the atmosphere, other processes such as subgrid-scale turbulent mixing cannot be neglected, especially if tracers advected by (11) are to evolve consistently with the primary mass field variables that in FIM are subjected to subgrid-scale vertical mixing. At the end of each long transport step, the relevant ''physics'' equations therefore are solved for each tracer in question, using $J\Delta t$ as time step.

## 4. Model physics

### a. Brief summary of GFS physics for FIM

To facilitate comparison of FIM to existing operational NWP models, and in particular the GFS, column physics parameterizations have been taken directly from the 2011 version of the GFS (most current at that time). Additional information can be found in the references provided in the section below, from the GFS website (www.emc.ncep.noaa.gov/GFS/impl.php) and from presentations at the 2013 NOAA Environmental Modeling System (NEMS)/GFS Summer School website (www.earthsystemcog.org/projects/gfsmodelingschool/). The description below corresponds to the GFS physics configuration implemented in the operational GFS model in 2011.

The physics routines are typically not executed at every dynamical time step. An individual physics routine produces tendencies (e.g., $\partial\theta/\partial t$) from the particular process being represented. The tendencies can either be used to increment the state variables instantaneously (and hence intermittently) or they can be passed to the dynamical equations where they are applied at each dynamical time step. The former option is presently taken.

Both longwave (LW) and shortwave (SW) radiation schemes make use of the rapid radiative transfer model (RRTM; Mlawer et al. 1997). Both LW and SW schemes account for the presence of a climatological distribution of atmospheric aerosols. The LW scheme includes effects of ozone, water vapor, and carbon dioxide as well as less radiatively important constituents such as methane, $NO_x$, and up to four types of halocarbons. Effects of clouds are either from a cloud fraction specification based on static stability and relative humidity or incorporated directly through a computed cloud liquid or ice path and an assumed effective radius for condensate produced by the microphysics scheme (see below). A maximum random cloud overlap scheme (Iacono et al. 2000) is used.

Land surface processes are simulated by the NCEP Noah land surface model (LSM); see Koren et al. (1999) and Ek et al. (2003) for an approximate description of the version of the Noah LSM implemented in the operational GFS in 2011. The Noah scheme uses four soil layers having lower boundaries at 10-, 40-, 100-, and 200-cm depth. Surface emissivity is reduced by 5% over snow, taking into account the snow-cover fraction. The surface latent heat flux has three components: flux from bare soil, evaporation of water from the vegetation canopy, and transpiration. The canopy resistance in evapotranspiration depends on solar radiation, temperature, humidity, and soil moisture. Monin–Obukhov similarity is used in the GFS surface layer scheme to calculate stability-dependent friction velocities and exchange coefficients over land surfaces. These variables are passed into the land surface model for calculating surface momentum fluxes as well as sensible and latent heat fluxes. Surface parameters are based on the MODIS land cover classification.

Turbulent mixing above the surface layer is parameterized following Hong and Pan (1996) based on Troen and Mahrt (1986) but with modifications to better account for enhanced cloud top–driven mixing when low clouds are present (Han and Pan 2011).

Gravity wave drag in the GFS physics package is parameterized based on Alpert et al. (1988), with enhancements to account for wind direction and subgrid terrain effects following Kim and Arakawa (1995).

The effects of moist convection on the explicitly predicted variables are incorporated through either a shallow or a deep parameterization scheme (Han and Pan 2011). Both schemes are mass flux schemes, with updrafts and downdrafts represented as entraining and detraining plumes. If conditional instability is limited in vertical extent, the parameterized convection is assumed to be ''shallow'' (cloud thickness $< 150$ hPa for shallow convection) with a large entrainment and detrainment rate for the updraft, and cloud top is constrained to be near or below the level where pressure is approximately 70% of surface pressure. The updraft mass flux at cloud base in the shallow convection scheme is proportional to the convective velocity scale $w^*$. For deeper instability, the so-called simplified Arakawa–Schubert (SAS) parameterization of deep convection is used. The SAS has been changed extensively (Han and Pan 2006, 2011), subsequent to the Grell (1993) modification of the original Arakawa and Schubert (1974) formulation, and now assumes that updraft entrainment decreases with height above cloud base, while detrainment extends through the depth of the updraft instead of occurring only near the cloud top. Unlike many shallow convection schemes,

light precipitation is also allowed to occur from the parameterized shallow convection.

For reasons of computational efficiency, grid-scale cloud condensate for both water and ice is combined in GFS (and FIM) into a total cloud condensate variable, which is advected as a tracer in FIM. At present, it, like $\theta$, is advected at every model time step. The treatment of cloud condensate and grid-scale precipitation follows closely Zhao and Carr (1997). Cloud condensate has two sources: detrainment of condensate from (parameterized) shallow and deep convection updrafts and grid-scale condensation, which is allowed to occur at relative humidity values slightly under 100%. The sinks of cloud condensate are grid-scale conversion of cloud to precipitation and evaporation. Precipitation processes are assumed to be appropriate for ice (Zhao and Carr 1997) or liquid (Sundqvist et al. 1989) depending on temperature.

### b. Discussion

In the course of importing the GFS physics into FIM, no changes have been made to any code or parameters. This allows for a clean comparison regarding the dynamic cores used in GFS and FIM. To properly link FIM to GFS physics, three additional 3D prognostic variables had to be added to FIM, namely, mixing ratios of water vapor, condensate, and ozone.

Within the GFS, the physics routines operate on individual grid columns, independently of adjacent columns, with the vertical discretization being determined by the GFS vertical coordinate. In our application of the GFS physics, we use FIM's ALE discretization directly, rather than interpolating back and forth between two grids. Within the isentropic portion of the grid domain, that is, well above the surface except in very cold areas, the hybrid vertical coordinate can possess much larger variability in layer thickness than the GFS because of static stability variations in the vertical and the particular distribution of the target $\theta$ values. The thickness of individual model layers typically also varies horizontally, particularly as these layers encounter upper fronts or the tropopause. This circumstance has not led to systematic errors in FIM of which we are aware, as will be shown in Part II of this paper. However, we did discover a vulnerability in the shallow and deep convection codes stemming from the variability in thickness of the ALE coordinate: with their assumed constant updraft detrainment rates and decreasing entrainment rates with height, the updrafts could, in effect, ''run out of mass'' upon encountering a thick isentropic layer. With concurrence from S. Moorthi (NCEP, 2011, personal communication), we introduced a generalization into the GFS code to deal with this issue in a physically consistent fashion.

### c. $T$–$\theta$ conversion and midlayer pressure definition

Temperature is not a prognostic variable in FIM and hence must be inferred from $\theta$ and $p$ when needed. Since model ''dynamics'' in FIM are formulated in terms of $\theta$ while model physics are formulated predominantly in terms of $T$, the $\theta/T$ conversion takes place frequently and in both directions. To avoid numerical degradation during this frequent back and forth, we define $T$, like $\theta$, as a layer variable and solve physics equations in layers, not on interfaces.

There appears to be considerable freedom in how to define a ''layer'' pressure or layer Exner function, needed for relating $\theta$ to $T$. One particularly compelling and widely used choice [e.g., Sela 1980, their Eq. (10); Arakawa and Lamb 1977, their Eq. (250)] is based on the notion that the column integral for the sum of potential and internal energy should not depend on whether it is evaluated numerically in terms of $\theta$ or in terms of $T$. The two forms of the integral (with the effect of water vapor only captured approximately) are

$$\frac{c_p}{g}\int T\,dp = \frac{c_p p_0}{g(1+\kappa)}\int \theta d\left(\frac{p}{p_0}\right)^{1+\kappa} \tag{12}$$

where $\kappa = R/c_p$. Equality is assured if

$$\frac{\theta}{1+\kappa} d\left(\frac{p}{p_0}\right)^{1+\kappa} = T d\left(\frac{p}{p_0}\right)$$

in each model layer. This condition is met if the Exner function value relating $\theta$ to $T$ in a model layer is defined as a finite-difference analog of

$$\frac{c_p}{1+\kappa}\frac{\partial(p/p_0)^{1+\kappa}}{\partial(p/p_0)}.$$

By satisfying (12), the model correctly translates temperature changes resulting from, for example, radiation or water phase changes into available potential energy changes in the dynamics part of FIM where they are represented in terms of $\theta$.

## 5. Sequence of operations

Variables are updated during each model time step in the following order:

1) Starting from momentum $\mathbf{v}^n$ and layer thickness $\Delta p^n$ at time level $n$, preliminary values at time level $n+1$ are obtained in each layer by solving (5) and (6) under the assumption that all interfaces are material ($\dot{s}=0$). We refer to the resulting values as $\mathbf{v}_{\rm sw}^{n+1}$, $\Delta p_{\rm sw}^{n+1}$ where

subscript sw stands for shallow water, a reminder that the two-dimensional versions of the respective prognostic equations have been used.

2) Thermal energy ($\theta\Delta p$) is advanced in time by solving (7), once again with $\dot{s}$ set to zero, and with the right-hand side set to zero. The outcome of this process is $(\theta\Delta p)^{n+1}_{\rm sw}$.
3) Values of $\theta^{n+1}_{\rm sw}$ are obtained by dividing $(\theta\Delta p)^{n+1}_{\rm sw}$ resulting from step 2 by $\Delta p^{n+1}_{\rm sw}$. Safeguards are applied to avoid indeterminacies in the limit of zero layer thickness.
4) Diabatic forcing due to radiation, surface fluxes, release of latent heat, and so on are evaluated using the GFS physical parameterization module based on $\theta^{n+1}_{\rm sw}$, $\Delta p^{n+1}_{\rm sw}$, and other state variables at time level $n + 1$. These calculations yield updated state variables, including $\theta^{n+1}_{\rm phy}$, where phy stands for model physics.
5) Fields of $\theta^{n+1}_{\rm phy}$, $\Delta p^{n+1}_{\rm sw}$ are fed to the grid generator that decides on the magnitude of interface fluxes $\dot{s}\partial p/\partial s$ at each grid point. These flux values are used to evaluate the missing vertical advection terms in (5), (6), and (7), yielding final values $\mathbf{v}^{n+1}$, $\Delta p^{n+1}$, $\theta^{n+1}$, and other state variables.

Other variables carried by the model to define the physical state of the atmosphere (mixing ratio of water vapor and hydrometeors, etc.) are advanced in time like the variable $\theta$. This is to say that transport takes place in flux form analogously to (7), source terms are evaluated as in step 4, and the variables are advected vertically as part of step 5.

Vertical advection of model variables, only necessary in regions where $p^{n+1}_{\rm sw} \neq p^{n+1}$, is implemented as a vertical remapping of the stairstep profiles resulting from the preliminary shallow-water integration. To remain stable in situations where layer thickness approaches zero while $\dot{s}\partial p/\partial s$ remains finite, the remapping algorithms PCM, PLM, and PPM available in FIM are formulated to allow (vertical) Courant numbers $> 1$. However, in the interest of computational efficiency, we no longer allow grid points to migrate outside the interval spanned by the $p_{\rm sw}$ values immediately above and below. This is equivalent to limiting the Courant number to 1.

## 6. Model initialization and postprocessing

Initial conditions for FIM are presently based on fields provided by NOAA's Global Forecast System. The state of the atmosphere is represented in that system by layer averages of virtual temperature, humidity, ozone mixing ratio, and horizontal velocity components plus interface values of pressure and geopotential. The data describe conditions in 64 hybrid $\sigma$–$p$ layers on a Gaussian grid in the form of spherical spectral coefficients. These fields are transformed to the physical domain and are processed as follows:

1) Terrain height, interface pressure, and interface geopotential as well as layer averages of humidity, wind, and ozone mixing ratio are interpolated horizontally to the icosahedral grid using an efficient spherical linear interpolation scheme (Wang 2013).
2) Virtual potential temperature in the $\sigma$–$p$ layers on the icosahedral grid is deduced from pressure and geopotential, using the hydrostatic equation in the form

$$\partial\phi/\partial\Pi = -\theta. \tag{13}$$

Deriving $\theta$ from $\phi$ minimizes the risk of introducing hydrostatic inconsistencies during horizontal interpolation.
3) In each grid column on the icosahedral grid, the stairstep profile defined in terms of $\theta$ and $\Pi$ in the $\sigma$–$p$ system, to be referred to as $\theta_{\rm in}(\Pi)$, is converted into a new stairstep profile $\theta_{\rm out}(\Pi)$ in which the "risers" are the prescribed $\theta$ coordinate values. The elevations of the "landings," carpenter's term for the horizontal sections in $\theta_{\rm out}(\Pi)$, are the unknowns in this problem.

   The transformation, which we refer to as "restepping" and which is described more fully in Bleck et al. (2010), can result in the formation of one or more zero thickness layers at the top and bottom of the column. Those will be inflated in the next step.

   To minimize truncation problems while converting one stairstep profile into another, the restepping process is broken into two steps. First, the piecewise constant profile $\theta_{\rm in}(\Pi)$ is converted into a continuous, piecewise linear profile using an extension of the integral-conserving method described in Bleck (1984). The linear segments are then integrated piecewise to form a stairstep profile with risers in the desired places.

   Use of the Exner function $\Pi$ as opposed to $p$ as vertical coordinate guarantees that the height $\int \theta\, d\Pi$ of the input column is preserved during each step of the vertical coordinate transform. Without this constraint, large-amplitude external gravity waves would likely be excited in the model at the beginning of the forecast.
4) The grid generator is invoked to inflate zero thickness layers at the surface and the top that may have been generated while transforming the original $\sigma$–$p$ layers to isentropic layers. The piecewise linear $\theta$ profile in the column is then integrated

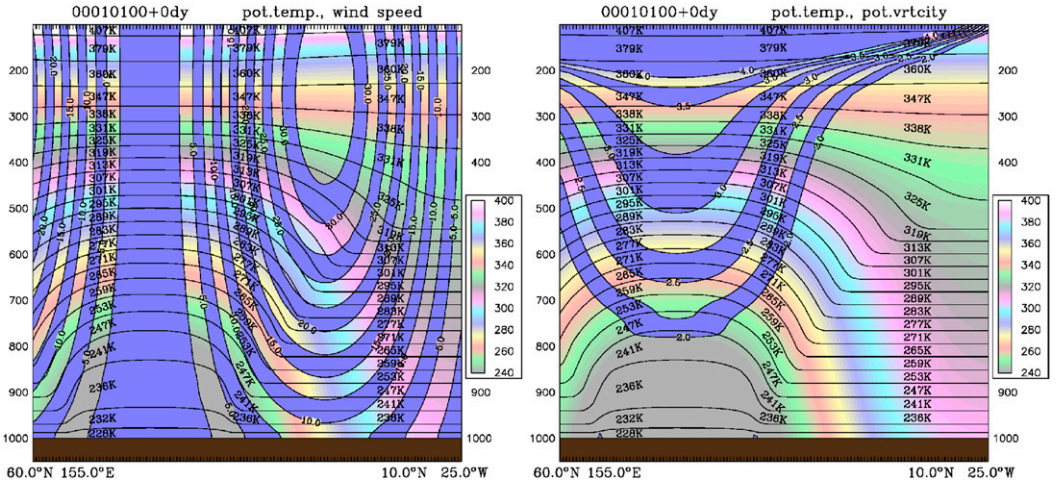


FIG. 2. Zonally symmetric initial conditions in baroclinic wave test. The meridional sections extend from 60°N (left edge) across the pole to 10°N (right edge) and from 1050 to 100 hPa in the vertical. Contours accentuated by blue striping: (left) velocity and (right) potential vorticity (contours > 5 ppvu omitted). Rainbow colors indicate potential temperature (K). Also shown are layer interfaces (solid) and target $\theta$ values (numbers ending on K) in each layer.

over the newly formed layers to generate layer mean values.

5) Moisture, ozone mixing ratio, and velocity components are expanded into piecewise linear profiles and then integrated over the hybrid $\sigma$–$\theta$ coordinate layers resulting from the previous step.
6) Fields of Montgomery potential are obtained by integrating the hydrostatic equation [(4)]. Integration starts with $M$ defined in the lowest layer as $M_1 = \Pi_{\rm sfc}\theta_1 + \phi_{\rm sfc}$, where $\theta_1$ is the virtual potential temperature in layer one and sfc stands for values at ground level.

For display purposes and other offline processing, forecast fields are interpolated to $p$ coordinates and to a standard latitude–longitude mesh. The vertical interpolation scheme takes into account the fact that most variables are treated by the model numerics as piecewise constant with discontinuities at layer interfaces. The discontinuities are reduced prior to vertical interpolation by replacing the risers in the stairstep profiles by slanted segments whose slopes are constrained to avoid sawtoothlike overshoots.

The geopotential on $p$ surfaces is obtained by hydrostatic integration from the nearest interface, using (13). The integral $\int \theta\, d\Pi$ is evaluated using slanted $\theta$ risers that therefore must be constructed in Exner function space for hydrostatic consistency.

## 7. A simple illustration of model performance: Rossby wave breaking

As stated earlier, emphasis in Part I of this paper is on model documentation, while Part II will focus on the performance of FIM in real data forecasting. However, for the convenience of readers not particularly interested in real data applications, we include here results from a model test developed by Jablonowski and Williamson (2006, hereinafter JW06) that deals with baroclinic instability in zonal flow on the sphere.

Emphasis will be on the impact of FIM's hybrid-isentropic vertical coordinate—the feature that sets FIM apart from most other models, more so than the icosahedral horizontal grid. Our aim is to explore, in admittedly cursory fashion, the sensitivity of the test solution to the choice of vertical coordinate.

The basic state used in this test, representing baroclinically unstable midlatitude zonal flow in both hemispheres, is documented in the JW06 article for the case of 26 model layers. Following Ullrich et al. (2012), we increased the number of layers to 30 and chose an icosahedral grid of roughly 120-km mesh size. Figure 2 shows the salient aspects of the initial fields in the latitude range of interest for the 30-layer model configuration. The figure also illustrates the placement of the hybrid $\sigma$–$\theta$ coordinate layers and shows the $\theta$ target value assigned to each coordinate layer.

Rossby waves owe their existence to lateral gradients of potential vorticity (PV) in the ambient flow field. (In the simplest case, the planetary $\beta$ effect provides the PV gradient.) Baroclinic instability is one of several possible mechanisms exciting Rossby waves. When these waves become large enough, they often are observed to break (McIntyre and Palmer 1985), at which stage the associated cyclones and anticyclones, the trademark of baroclinic instability, cease to develop and acquire an equivalent-barotropic character.

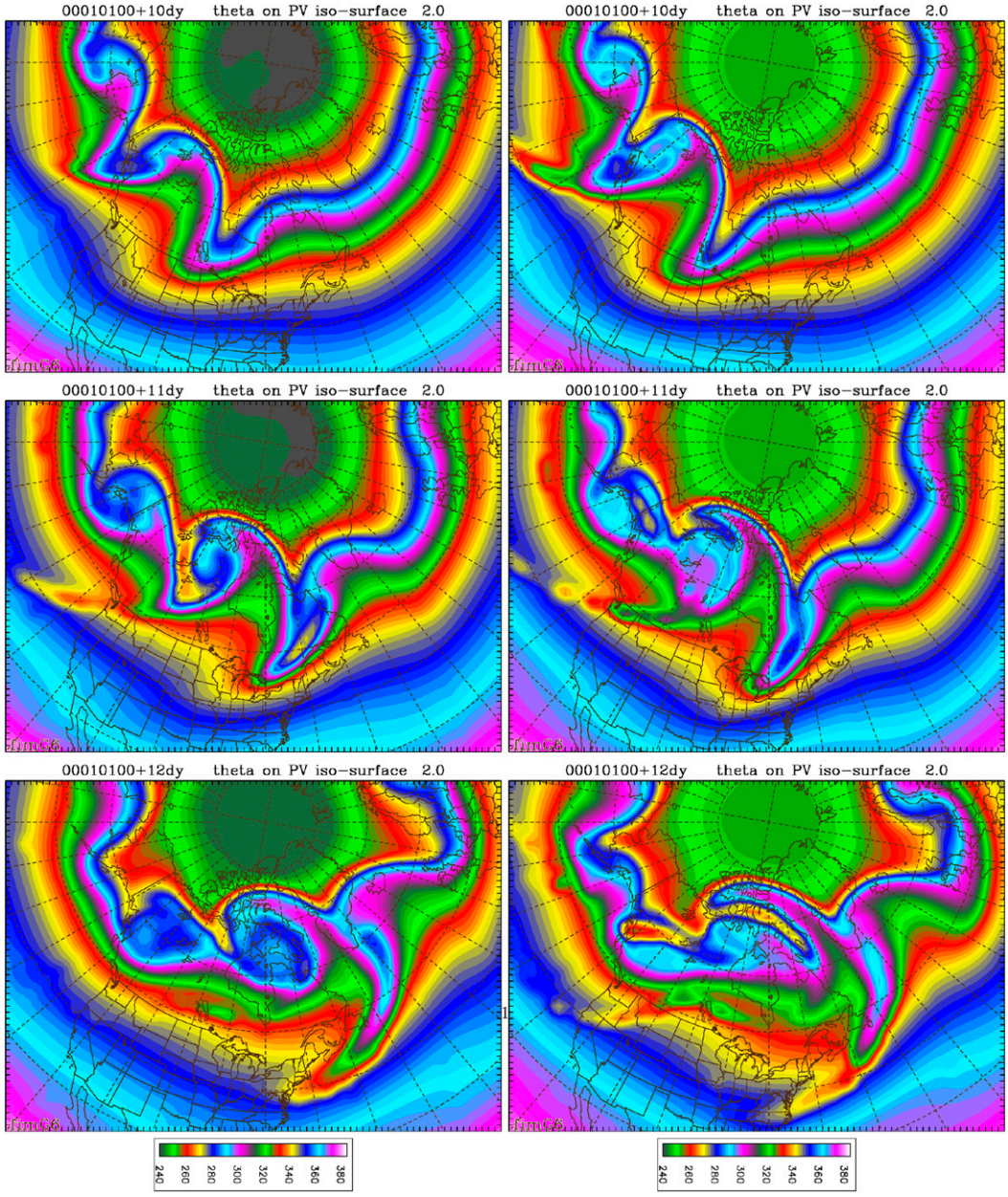


FIG. 3. Potential temperature (K) on the PV = 2 ppvu surface on days 10–12. Mesh size is 120 km and 30 layers. (left) Hybrid $\sigma$–$\theta$ coordinate simulation; (right) pure $\sigma$ coordinate simulation.

The process of Rossby wave breaking is of interest because the resulting regional homogenization of PV creates a favorable environment for longer-lived eddies, such as those contributing to atmospheric blocking of midlatitude flow (Rex 1950; Pelly and Hoskins 2003).

Given the importance of PV, we show its initial distribution in Fig. 2 and conclude, as do JW06, that the pattern is sufficiently realistic. PV is defined here as the hydrostatic rendition of "Ertel" PV:

$$\mathrm{PV} = \left(\frac{\partial\theta}{\partial p}\right)(\zeta_\theta + f) \tag{14}$$

and is expressed in practical PV units (1 ppvu = $10^{-6}\,\mathrm{K\,Pa^{-1}\,s^{-1}}$).

Converting vorticity diagnosed in nonisentropic coordinates to $\zeta_\theta$ has been found to introduce noise in the PV plots that viewers are likely to find distracting. Therefore, we approximate $\zeta_\theta$ in (14) by the vorticity $\zeta_s$ evaluated on the native grid. This approximation is

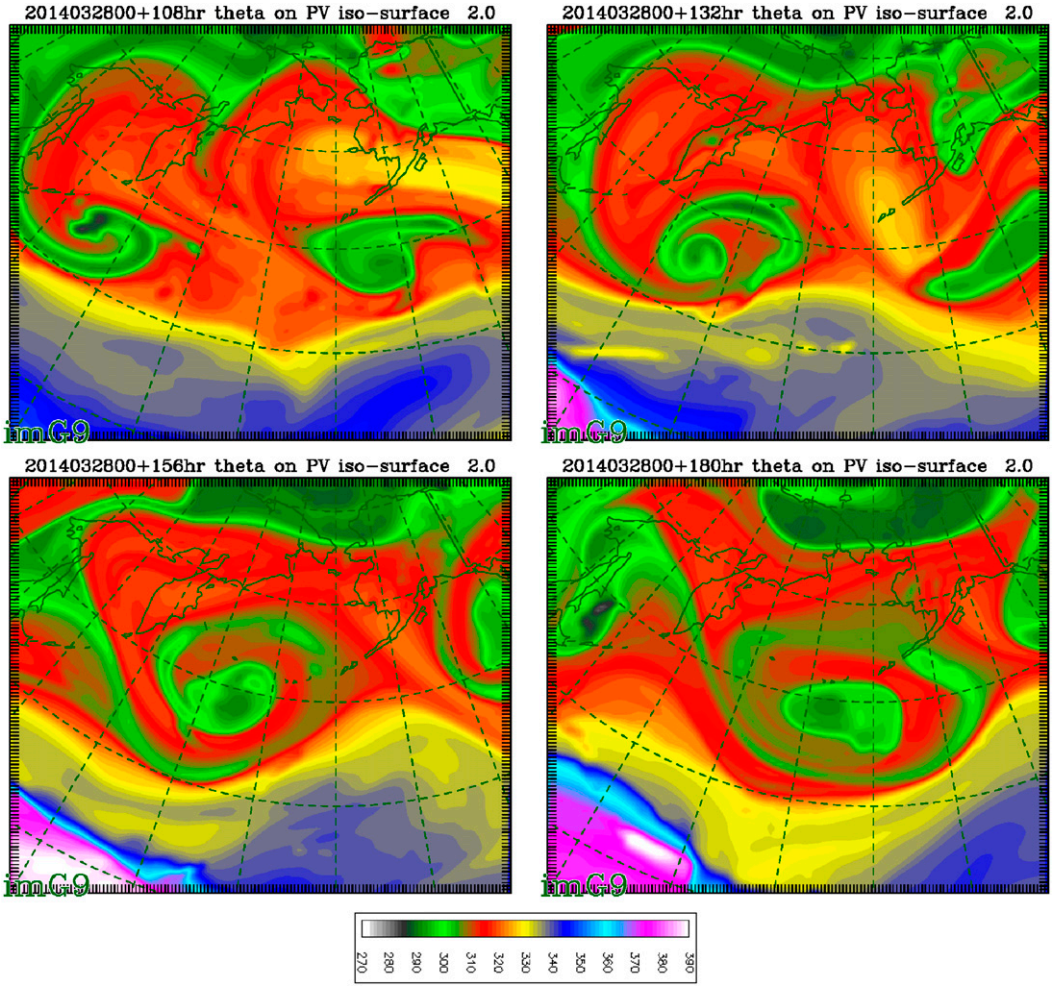


FIG. 4. Potential temperature (K) on the PV = 2 ppvu surface over the Pacific at 24-h intervals in a forecast initialized at 0000 UTC 28 Mar 2014. Hybrid $\sigma$–$\theta$ coordinate simulation, mesh size is 15 km and 64 layers.

insignificant compared to the much larger truncation error associated with evaluating the stratification factor $\partial\theta/\partial p$ in nonisentropic coordinates.

Rossby wave breaking is best illustrated by the evolution of the $\theta$ field on a tropopause-level PV surface (e.g., Pelly and Hoskins 2003; Masato et al. 2012). Plotting $\theta$ on a PV surface, rather than PV on a $\theta$ surface, has the practical advantage of displaying conditions on a surface that tends to track the tropopause and hence approximates at most latitudes the level where Rossby waves in an equivalent-barotropic atmosphere reach their maximum amplitude.

Steps taken to prevent ambiguities in columns where the PV field is not vertically monotonic, a frequent occurrence in highly resolved isentropic grids (as well as in nature), are outlined in the appendix.

Baroclinic development of the JW06 test is triggered by a localized barotropic perturbation of the zonal wind field. This perturbation is unlikely to project well onto any unstable baroclinic mode of the background flow. Consequently, the model needs more than one week to sort things out, that is, develop a perturbation with a vertical phase lag appropriate for baroclinic growth. From that stage on, development is rapid, with surface cyclones deepening by as much as 50 hPa.

We focus on days 10–12 of the simulation. The instability process at this time has created a series of surface cyclones and anticyclones in various stages of development (not shown here). Aloft, we see in the left-hand panels of Fig. 3 a corresponding train of breaking Rossby waves. (Continental outlines have been added to these figures to provide a real-world context to the JW06 simulation; they do not imply a land–sea contrast in surface boundary conditions.)

Space limitations only permit a brief look at another simulation in which the standard FIM coordinate was

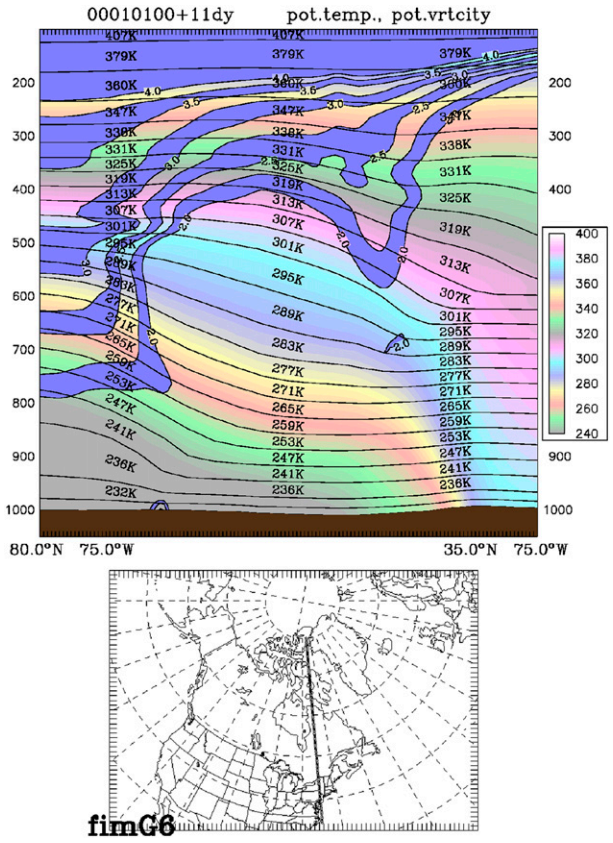


FIG. 5. Sample meridional section taken from day 11 of the hybrid $\sigma$–$\theta$ simulation of the JW06 test case, showing two stratospheric extrusions generated in the course of the baroclinic instability process. See Fig. 2 for other details. Location of cross section is indicated by heavy line in bottom panel.

replaced by a pure $\sigma$ coordinate, using the 30 $\sigma$ values prescribed in Table XVIII of Ullrich et al. (2012).

Tropopause-level features corresponding timewise to those in the left-hand panels of Fig. 3 are shown in the right-hand panels. As one would expect, the wave breaking process is simulated more cleanly in the simulation benefitting from isentropic coordinate representation (left panels). Explicit, and by virtue of the vertical isentropic grid fairly accurate, prediction of the inverse of the stratification term $\partial\theta/\partial p$ in (14) [see (1)] very likely enhances the fidelity of the PV field and its evolution.

Spiraling of high PV streamers (depicted here as low $\theta$ streamers) during wave breaking is clearly visible in the lower panels on the left side of Fig. 3. In real data simulations conducted with higher-resolution versions of FIM (64 layers on 15- or 30-km meshes), we occasionally see such streamers making two or more full revolutions. A striking example is shown in Fig. 4.

Note that the unstaggered grid used in FIM does not allow construction of finite-difference operators mimicking exact conservation of quantities like PV during transport. Nevertheless, the temporal coherence of low $\theta$ filaments encircling the vortex in Fig. 4 suggests that in the isentropic coordinate subdomain FIM comes fairly close to being PV conserving.

The process of Rossby wave breaking creates the familiar ''extrusions'' of lower-stratospheric air into the upper troposphere (Reed and Danielsen 1958; Shapiro et al. 1980). We show in Fig. 5 an example taken from the hybrid $\sigma$–$\theta$ coordinate simulation. It is worth noting that no vertical motion is needed to create these extrusions; they are a consequence of the lateral stirring process depicted in Fig. 3.

## 8. Conclusions

A hydrostatic global weather prediction model based on an icosahedral horizontal grid and an adaptive, primarily isentropic vertical grid has been described. The primitive equations are discretized in the model on the icosahedral equivalent of the A grid. The vertical grid continually adapts to maximize the portion of the atmosphere represented by isentropic coordinates. In the lower troposphere, the grid defaults to terrain-following ($\sigma$) coordinates. At the highest model levels, the grid likewise reverts to an isobaric grid; the intent here is to better control the damping of vertically propagating gravity waves in the meso- and upper stratosphere.

Horizontal finite-difference operations in FIM are based on the unstructured grid paradigm; this is to say that a lookup table is used to tell each grid cell who its neighbors are. While dividing the icosahedral grid into 10 logically rhomboidal areas makes it possible, in principle, to employ a direct addressing scheme inside each rhombus (Majewski et al. 2002), such an approach requires separate treatment of rhombus edges and of the 12 pentagons marking the corners of the icosahedron.

The decision to treat the icosahedral grid as unstructured is largely based on tests by MacDonald et al. (2011) that indicated that the time penalty for indirect addressing is inconsequential, at least in three-dimensional simulations. While table lookup does add a layer of complexity, the computer code for solving the prognostic equations in (5)–(7) ends up being more robust and transparent because the same finite-difference logic is used at all points on the sphere; furthermore, this approach permits easy implementation of different memory layouts for cache blocking, distributed memory parallelism, and load balancing. (In this context it is worth noting that horizontal grid resolution in FIM—that is, the number of icosahedral refinement steps—is user selectable at run time.)

We have shown a few results from an idealized test simulating baroclinic instability on the sphere to give the

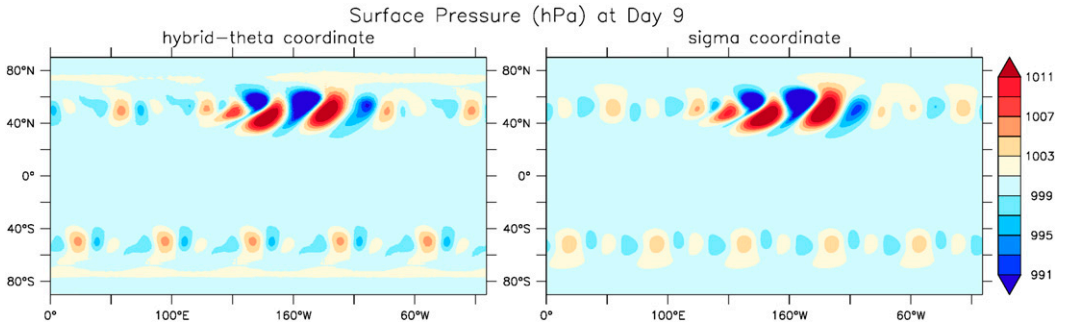


FIG. 6. Surface pressure (hPa) at day 9 in cylindrical equidistant projection. (left) Hybrid $\sigma$–$\theta$ simulation; (right) pure $\sigma$ simulation. Mesh size is 120 km.

reader a cursory impression of the model's capabilities. More test cases, as well as material relating to FIM's performance in the real data forecast realm, will be presented in Part II. Experimental, twice-daily, medium-range weather forecasts at 15- and 30-km horizontal grid resolution, which permit a detailed look at FIM's performance on a day-to-day basis, are posted online (http://fim.noaa.gov).

One issue discussed by JW06, Lauritzen et al. (2010), and Skamarock et al. (2012), among others, is the zonal variation of mesh size on cube- and icosahedron-based geodesic grids. In the icosahedral case, this variation imparts a miniscule but nonzero wavenumber-5 signal on the prescribed zonal flow. (Near the equator, there is also wavenumber-10 variability.) Planetary waves of that length are common in the atmosphere and are baroclinically unstable in the JW06 test. Given the long lead time required to convert the initially prescribed barotropic velocity perturbation into a proper unstable mode, it should not come as a surprise that these spurious waves appear in the solution. In fact, only in the 7–15-day time window are they overshadowed by the deliberately induced cyclogenesis event.

As shown in Fig. 6, unstable waves of wavenumber 5 (and to a lesser extent 10) have reached an amplitude of 4–5 hPa by day 9 in the JW06 baroclinic wave test. At that particular time, the amplitude is slightly higher in the $\sigma$–$\theta$ simulation, but the reverse is true for some other times and choices of target $\theta$ values we have experimented with. These results are commensurate with results obtained by other icosahedral models [see Lauritzen et al. (2010) and www.earthsystemcog.org/projects/dcmip-2012/]. We plan to further investigate the sensitivity of the wavenumber-5 growth rate on the choice of vertical coordinate (including choice of target $\theta$ values) by applying the method of Trevisan et al. (1988), which finds the fastest-growing linear mode in a numerical model, to a linearized version of the FIM dynamic core used in the JW06 test.

*Acknowledgments.* The authors acknowledge the assistance and guidance provided by staff at the National Centers for Environmental Prediction, U.S. Weather Service, during the process of linking FIM to the GFS physics suite.

## APPENDIX

### Diagnosing Potential Temperature on Folding PV Surfaces

Much of the spatial variability of the three-dimensional PV field is due to variations in the stratification factor $\partial\theta/\partial p$ in (14). Spatial details in $\partial\theta/\partial p$ captured in $\theta$ coordinates often yield PV fields that are multivalued in the vertical, particularly at tropopause level (tropopause folds). The scheme described in the following has been proven capable of generating meaningful values of $\theta$(PV) when PV equals the chosen reference value $\mathrm{PV}_o$ at more than one elevation.

With PV typically being small in the troposphere and large in the stratosphere, a judicious choice of $\mathrm{PV}_o$ will yield at least one level in the column where $\mathrm{PV}(p) = \mathrm{PV}_o$. To detect situations where several such levels exist, the algorithm determines the lowest and highest pressures, $p_{\mathrm{lo}}$ and $p_{\mathrm{hi}}$, where $\mathrm{PV}(p)$ matches $\mathrm{PV}_o$. If $\Delta p = p_{\mathrm{hi}} - p_{\mathrm{lo}} > 0$, indicating multivaluedness, the intervals where $\mathrm{PV}(p) > \mathrm{PV}_o$ and $\mathrm{PV}(p) < \mathrm{PV}_o$ inside the range $(p_{\mathrm{lo}}, p_{\mathrm{hi}})$ are summed up separately. This process yields two pressure subranges $\Delta p_+$, $\Delta p_-$ that add up to $\Delta p$. The weighted pressure

$$p_o = \frac{\Delta_+ p_{\mathrm{hi}} + \Delta_- p_{\mathrm{lo}}}{\Delta p}$$

is then taken as the level where $\mathrm{PV} = \mathrm{PV}_o$. The weighting assures that $p_o$ varies continuously among neighboring columns, thereby avoiding lateral $\theta(p_o)$ discontinuities in the vicinity of PV surface folds.

## REFERENCES


Alpert, J., M. Kanamitsu, M. Caplan, J. Sela, G. White, and E. Kalnay, 1988: Mountain induced gravity wave drag parameterization in the NMC MRF model. Preprints, *Eighth Conf. on Numerical Weather Prediction,* Baltimore, MD, Amer. Meteor. Soc., 726–733.

Arakawa, A., and W. H. Schubert, 1974: Interaction of a cumulus ensemble with the large-scale environment, Part I. *J. Atmos. Sci.,* **31,** 674–704, doi:10.1175/1520-0469(1974)031<0674:IOACCE>2.0.CO;2.

——, and V. R. Lamb, 1977: Computational design of the basic dynamical processes of the UCLA general circulation model. *General Circulation Models of the Atmosphere,* J. Change, Ed., Methods in Computational Physics, Vol. 17, Academic Press, 173–265, doi:10.1016/B978-0-12-460817-7.50009-4.

Baumgardner, J. R., and P. O. Frederickson, 1985: Icosahedral discretization of the two-sphere. *SIAM J. Numer. Anal.,* **22,** 1107–1115, doi:10.1137/0722066.

Benjamin, S., G. Grell, J. Brown, T. Smirnova, and R. Bleck, 2004: Mesoscale weather prediction with the RUC hybrid isentropic–terrain-following coordinate model. *Mon. Wea. Rev.,* **132,** 473–494, doi:10.1175/1520-0493(2004)132<0473:MWPWTR>2.0.CO;2.

Bleck, R., 1978: Finite difference equations in generalized vertical coordinates. Part I: Total energy conservation. *Beitr. Phys. Atmos.,* **51,** 360–372.

——, 1984: Vertical coordinate transformation of vertically-discretized atmospheric fields. *Mon. Wea. Rev.,* **112,** 2535–2539, doi:10.1175/1520-0493(1984)112<2535:NAC>2.0.CO;2.

——, 2002: An oceanic general circulation model framed in hybrid isopycnic-Cartesian coordinates. *Ocean Modell.,* **4,** 55–88, doi:10.1016/S1463-5003(01)00012-9.

——, and S. Benjamin, 1993: Regional weather prediction with a model combining terrain-following and isentropic coordinates. Part I: Model description. *Mon. Wea. Rev.,* **121,** 1770–1785, doi:10.1175/1520-0493(1993)121<1770:RWPWAM>2.0.CO;2.

——, ——, J. Lee, and A. E. MacDonald, 2010: On the use of an adaptive, hybrid-isentropic vertical coordinate in global atmospheric modeling. *Mon. Wea. Rev.,* **138,** 2188–2210, doi:10.1175/2009MWR3103.1.

Boris, J. P., and D. L. Book, 1973: Flux-corrected transport. I. SHASTA, a fluid transport algorithm that works. *J. Comput. Phys.,* **11,** 38–69, doi:10.1016/0021-9991(73)90147-2.

Chen, C.-C., and P. J. Rasch, 2012: Climate simulations with an isentropic finite-volume dynamical core. *J. Climate,* **25,** 2843–2861, doi:10.1175/2011JCLI4184.1.

Colella, P., and P. Woodward, 1984: The piecewise parabolic method (PPM) for gas-dynamical simulations. *J. Comput. Phys.,* **54,** 174–201, doi:10.1016/0021-9991(84)90143-8.

Cooley, J. W., and J. W. Tukey, 1965: An algorithm for the machine calculation of complex Fourier series. *Math. Comput.,* **19,** 297–301, doi:10.1090/S0025-5718-1965-0178586-1.

Du, Q., M. Gunzburger, and L. Ju, 2003: Voronoi-based finite volume methods, optimal Voronoi meshes, and PDEs on the sphere. *Comput. Methods Appl. Mech. Eng.,* **192,** 3933–3957, doi:10.1016/S0045-7825(03)00394-3.

Dubey, S., R. Mittal, and P. Lauritzen, 2014: A flux-form conservative semi-Lagrangian multitracer transport scheme (FF-CSLAM) for icosahedral-hexagonal grids. *J. Adv. Model. Earth Syst.,* **6,** 332–356, doi:10.1002/2013MS000259.

Durran, D. R., 1991: The third-order Adams–Bashforth method: An attractive alternative to leapfrog time differencing. *Mon. Wea. Rev.,* **119,** 702–720, doi:10.1175/1520-0493(1991)119<0702:TTOABM>2.0.CO;2.

Ek, M. B., K. E. Mitchell, Y. Lin, E. Rogers, P. Grunmann, V. Koren, G. Gayno, and J. D. Tarpley, 2003: Implementation of Noah land surface model advances in the National Centers for Environmental Prediction operational mesoscale Eta model. *J. Geophys. Res.,* **108,** 8851–8866, doi:10.1029/2002JD003296.

Gassmann, A., 2013: A global hexagonal C-grid non-hydrostatic dynamical core (ICON-IAP) designed for energetic consistency. *Quart. J. Roy. Meteor. Soc.,* **139,** 152–175, doi:10.1002/qj.1960.

Grell, G. A., 1993: Prognostic evaluation of assumptions used by cumulus parameterizations. *Mon. Wea. Rev.,* **121,** 764–787, doi:10.1175/1520-0493(1993)121<0764:PEOAUB>2.0.CO;2.

Han, J., and H.-L. Pan, 2006: Sensitivity of hurricane intensity forecast to convective momentum transport parameterization. *Mon. Wea. Rev.,* **134,** 664–674, doi:10.1175/MWR3090.1.

——, and ——, 2011: Revision of convection and vertical diffusion schemes in the NCEP Global Forecast System. *Wea. Forecasting,* **26,** 520–533, doi:10.1175/WAF-D-10-05038.1.

Heikes, R. H., and D. A. Randall, 1995a: Numerical integration of the shallow-water equations on a twisted icosahedral grid. Part I: Basic design and results of tests. *Mon. Wea. Rev.,* **123,** 1862–1880, doi:10.1175/1520-0493(1995)123<1862:NIOTSW>2.0.CO;2.

——, and ——, 1995b: Numerical integration of the shallow-water equations on a twisted icosahedral grid. Part II: A detailed description of the grid and analysis of numerical accuracy. *Mon. Wea. Rev.,* **123,** 1881–1887, doi:10.1175/1520-0493(1995)123<1881:NIOTSW>2.0.CO;2.

Hirt, C. W., A. A. Amsden, and J. L. Cook, 1974: An arbitrary Lagrangian-Eulerian computing method for all flow speeds. *J. Comput. Phys.,* **14,** 227–253, doi:10.1016/0021-9991(74)90051-5.

Hong, S.-Y., and H.-L. Pan, 1996: Nonlocal boundary layer vertical diffusion in a medium-range forecast model. *Mon. Wea. Rev.,* **124,** 2322–2339, doi:10.1175/1520-0493(1996)124<2322:NBLVDI>2.0.CO;2.

Iacono, M. J., E. J. Mlawer, and S. A. Clough, 2000: Application of a maximum-random cloud overlap method for RRTM to general circulation models. *Proc. 10th ARM Science Team Meeting,* San Antonio, TX, U.S. Dept. of Energy, 5 pp.

Jablonowski, C., and D. Williamson, 2006: A baroclinic instability test case for atmospheric model dynamical cores. *Quart. J. Roy. Meteor. Soc.,* **132,** 2943–2975, doi:10.1256/qj.06.12.

Janjic, Z. I., 1977: Pressure gradient force and advection scheme used for forecasting with steep and small scale topography. *Beitr. Phys. Atmos.,* **50,** 186–199.

Johnson, D. R., 1997: "General coldness of climate models" and the Second Law: Implications for modeling the Earth system. *J. Climate,* **10,** 2826–2846, doi:10.1175/1520-0442(1997)010<2826:GCOCMA>2.0.CO;2.

Kasahara, A., 1974: Various vertical coordinate systems used for numerical weather prediction. *Mon. Wea. Rev.,* **102,** 509–522, doi:10.1175/1520-0493(1974)102<0509:VVCSUF>2.0.CO;2.

Kim, Y.-J., and A. Arakawa, 1995: Improvement of orographic gravity wave parameterization using a mesoscale gravity wave model. *J. Atmos. Sci.,* **52,** 1875–1902, doi:10.1175/1520-0469(1995)052<1875:IOOGWP>2.0.CO;2.

Koren, V., J. Schaake, K. Mitchell, Q.-Y. Duan, F. Chenx, and J. M. Baker, 1999: A parameterization of snowpack and frozen ground intended for NCEP weather and climate models. *J. Geophys. Res.,* **104,** 19 569–19 585, doi:10.1029/1999JD900232.

Lauritzen, P. H., C. Jablonowski, M. A. Taylor, and R. D. Nair, 2010: Rotated versions of the Jablonowski steady-state and baroclinic wave test cases: A dynamical core intercomparison. *J. Adv. Model. Earth Syst.,* **2** (15), doi:10.3894/JAMES.2010.2.15.

Lee, J.-L., and A. E. MacDonald, 2009: A finite-volume icosahedral shallow water model on local coordinate. *Mon. Wea. Rev.,* **137,** 1422–1437, doi:10.1175/2008MWR2639.1.

——, R. Bleck, and A. E. MacDonald, 2010: A multistep flux-corrected transport scheme. *J. Comput. Phys.,* **229,** 9284–9298, doi:10.1016/j.jcp.2010.08.039.

Lin, S.-J., 2004: A vertically Lagrangian finite-volume dynamical core for global models. *Mon. Wea. Rev.,* **132,** 2293–2307, doi:10.1175/1520-0493(2004)132<2293:AVLFDC>2.0.CO;2.

——, W. C. Chao, Y. C. Sud, and G. K. Walker, 1994: A class of the van Leer-type transport schemes and its application to the moisture transport in a general circulation model. *Mon. Wea. Rev.,* **122,** 1575–1593, doi:10.1175/1520-0493(1994)122<1575:ACOTVL>2.0.CO;2.

MacDonald, A. E., J. L. Lee, and S. Sun, 2000: QNH: Design and test of a quasi-nonhydrostatic model for mesoscale weather prediction. *Mon. Wea. Rev.,* **128,** 1016–1036, doi:10.1175/1520-0493(2000)128<1016:QDATOA>2.0.CO;2.

——, J. Middlecoff, T. Henderson, and J.-L. Lee, 2011: A general method for modeling on irregular grids. *Int. J. High Perform. Comput. Appl.,* **25,** 392–403, doi:10.1177/1094342010385019.

Majewski, D., D. Liermann, P. Prohl, B. Ritter, M. Buchhold, T. Hanisch, G. Paul, and W. Wergen, 2002: The operational global icosahedral–hexagonal gridpoint model GME: Description and high-resolution tests. *Mon. Wea. Rev.,* **130,** 319–338, doi:10.1175/1520-0493(2002)130<0319:TOGIHG>2.0.CO;2.

Masato, G., B. J. Hoskins, and T. J. Woollings, 2012: Wave-breaking characteristics of midlatitude blocking. *Quart. J. Roy. Meteor. Soc.,* **138,** 1285–1296, doi:10.1002/qj.990.

Masuda, Y., and H. Ohnishi, 1987: An integration scheme of the primitive equation model with an icosahedral-hexagonal grid system and its application to the shallow water equations. *WMO/IUGG NWP Symp.: Short- and Medium-Range Numerical Weather Prediction,* Tokyo, Japan, Meteorological Society of Japan, 317–326.

McDougall, T. J., and W. K. Dewar, 1998: Vertical mixing and cabbeling in layered models. *J. Phys. Oceanogr.,* **28,** 1458–1480, doi:10.1175/1520-0485(1998)028<1458:VMACIL>2.0.CO;2.

McIntyre, M. E., and T. N. Palmer, 1985: A note on the general concept for wave braking of gravity and Rossby waves. *Pure Appl. Geophys.,* **123,** 964–975, doi:10.1007/BF00876984.

Mlawer, E. J., S. J. Taubman, P. D. Brown, M. J. Iacono, and S. Clough, 1997: Radiative transfer for inhomogeneous atmospheres: RRTM, a validated correlated-*k* model for the longwave. *J. Geophys. Res.,* **102,** 16 663–16 682, doi:10.1029/97JD00237.

Peixoto, P. S., and S. R. M. Barros, 2013: Analysis of grid imprinting on geodesic spherical icosahedral grids. *J. Comput. Phys.,* **237,** 61–78, doi:10.1016/j.jcp.2012.11.041.

Pelly, J. L., and B. J. Hoskins, 2003: A new perspective on blocking. *J. Atmos. Sci.,* **60,** 743–755, doi:10.1175/1520-0469(2003)060<0743:ANPOB>2.0.CO;2.

Pulido, M., and J. Thuburn, 2006: Gravity-wave drag estimation from global analyses using variational data assimilation principles. II: Case study. *Quart. J. Roy. Meteor. Soc.,* **132,** 1527–1543, doi:10.1256/qj.05.43.

Randall, D. A., T. D. Ringler, and R. Heikes, 2000: Global atmospheric modeling using a geodesic grid and an isentropic vertical coordinate. *General Circulation Model Development,* D. A. Randall, Ed., International Geophysics Series, Vol. 70, 509–536, doi:10.1016/S0074-6142(00)80065-0.

Reed, R. J., and E. F. Danielsen, 1958: Fronts in the vicinity of the tropopause. *Arch. Meteor. Geophys. Bioklimatol.,* **11,** 1–17, doi:10.1007/BF02247637.

Rex, D., 1950: Blocking action in the middle troposphere and its effect upon regional climate. *Tellus,* **2,** 196–211, doi:10.1111/j.2153-3490.1950.tb00331.x.

Ringler, T. D., R. P. Heikes, and D. A. Randall, 2000: Modeling the atmospheric general circulation using a spherical geodesic grid: A new class of dynamical cores. *Mon. Wea. Rev.,* **128,** 2471–2490, doi:10.1175/1520-0493(2000)128<2471:MTAGCU>2.0.CO;2.

——, D. Jacobsen, M. Gunzburger, L. Ju, M. Duda, and W. Skamarock, 2011: Exploring a multiresolution modeling approach with the shallow-water equations. *Mon. Wea. Rev.,* **139,** 3348–3368, doi:10.1175/MWR-D-10-05049.1.

Sadourny, R., A. Arakawa, and Y. Mintz, 1968: Integration of the nondivergent barotropic vorticity equation with an icosahedral-hexagonal grid for the sphere. *Mon. Wea. Rev.,* **96,** 351–356, doi:10.1175/1520-0493(1968)096<0351:IOTNBV>2.0.CO;2.

Satoh, M., T. Matsuno, H. Tomita, H. Miura, T. Nasuno, and S. Iga, 2008: Nonhydrostatic Icosahedral Atmospheric Model (NICAM) for global cloud resolving simulations. *J. Comput. Phys.,* **227,** 3486–3514, doi:10.1016/j.jcp.2007.02.006.

Schaack, T. K., T. H. Zapotocny, A. J. Lenzen, and D. R. Johnson, 2004: Global climate simulation with the University of Wisconsin global hybrid isentropic coordinate model. *J. Climate,* **17,** 2998–3016, doi:10.1175/1520-0442(2004)017<2998:GCSWTU>2.0.CO;2.

Sela, J. G., 1980: Spectral modeling at the National Meteorological Center. *Mon. Wea. Rev.,* **108,** 1279–1292, doi:10.1175/1520-0493(1980)108<1279:SMATNM>2.0.CO;2.

Shapiro, M. A., E. R. Reiter, R. D. Cadle, and W. A. Sedlacek, 1980: Vertical mass- and trace constituent transports in the vicinity of jet streams. *Arch. Meteor. Geophys. Bioklimatol.,* **28,** 193–206, doi:10.1007/BF02245351.

Skamarock, W. C., J. B. Klemp, M. G. Duda, L. D. Fowler, S.-H. Park, and T. D. Ringler, 2012: A multiscale atmospheric model using centroidal Voronoi tessellations and C-grid staggering. *Mon. Wea. Rev.,* **140,** 3090–3105, doi:10.1175/MWR-D-11-00215.1.

Staniforth, A., and J. Thuburn, 2012: Horizontal grids for global weather and climate prediction models: A review. *Quart. J. Roy. Meteor. Soc.,* **138,** 1–26, doi:10.1002/qj.958.

Sun, S., and R. Bleck, 2006: Geographic distribution of the diapycnal component of thermohaline circulations in coupled climate models. *Ocean Modell.,* **15,** 177–199, doi:10.1016/j.ocemod.2006.05.002.

Sundqvist, H., E. Berge, and J. E. Kristjansson, 1989: Condensation and cloud studies with mesoscale numerical weather prediction model. *Mon. Wea. Rev.,* **117,** 1641–1657, doi:10.1175/1520-0493(1989)117<1641:CACPSW>2.0.CO;2.

Thuburn, J., 1997: A PV-based shallow-water model on a hexagonal–icosahedral grid. *Mon. Wea. Rev.,* **125,** 2328–2347, doi:10.1175/1520-0493(1997)125<2328:APBSWM>2.0.CO;2.

Tomita, H., M. Tsugawa, M. Satoh, and K. Goto, 2001: Shallow water model on a modified icosahedral geodesic grid by using spring dynamics. *J. Comput. Phys.,* **174,** 579–613, doi:10.1006/jcph.2001.6897.

——, M. Satoh, and K. Goto, 2004: A new dynamical framework of global nonhydrostatic model using the icosahedral grid. *Fluid Dyn. Res.,* **34,** 357–400, doi:10.1016/j.fluiddyn.2004.03.003.

Trevisan, A., L. Ferranti, and P. Malguzzi, 1988: Further development of normal mode theory of lee cyclogenesis: Isentropic coordinate model. *J. Atmos. Sci.,* **45,** 3880–3888, doi:10.1175/1520-0469(1988)045<3880:FDONMT>2.0.CO;2.

Troen, I., and L. Mahrt, 1986: A simple model of the atmospheric boundary layer; sensitivity to surface evaporation. *Bound.-Layer Meteor.,* **37,** 129–148, doi:10.1007/BF00122760.

Ullrich, P. A., C. Jablonowski, J. Kent, P. H. Lauritzen, R. D. Nair, and M. A. Taylor, 2012: Dynamical Core Model Intercomparison Project (DCMIP) test case document. DCMIP Summer School, 83 pp. [Available online at https://earthsystemcog.org/site_media/docs/DCMIP-TestCaseDocument_v1.7.pdf.]

van Leer, B., 1974: Towards the ultimate conservative difference scheme. II. Monotonicity and conservation combined in a second order scheme. *J. Comput. Phys.,* **14,** 361–370, doi:10.1016/0021-9991(74)90019-9.

——, 1977: Towards the ultimate conservative difference scheme. III. Upstream-centered finite-difference schemes for ideal compressible flow. *J. Comput. Phys.,* **23,** 263–275, doi:10.1016/0021-9991(77)90094-8.

Wang, N., 2013: An efficient search algorithm for minimum covering polygons on the sphere. *SIAM J. Sci. Comput.,* **35,** A1669–A1688, doi:10.1137/120880331.

——, and J.-L. Lee, 2011: Geometric properties of the icosahedral-hexagonal grid on the two-sphere. *SIAM J. Sci. Comput.,* **33,** 2536–2559, doi:10.1137/090761355.

Webster, S., J. Thuburn, B. J. Hoskins, and M. J. Rodwell, 1999: Further development of a hybrid-isentropic GCM. *Quart. J. Roy. Meteor. Soc.,* **125,** 2305–2331, doi:10.1002/qj.49712555817.

Williamson, D., 1968: Integration of the barotropic vorticity equation on a spherical geodesic grid. *Tellus,* **20,** 642–653, doi:10.1111/j.2153-3490.1968.tb00406.x.

Zalesak, S., 1979: Fully multidimensional flux-corrected transport algorithms for fluids. *J. Comput. Phys.,* **31,** 335–362, doi:10.1016/0021-9991(79)90051-2.

Zängl, G., D. Reinert, P. Ripodas, and M. Baldauf, 2015: The ICON (ICOsahedral Non-hydrostatic) modelling framework of DWD and MPI-M: Description of the non-hydrostatic dynamical core. *Quart. J. Roy. Meteor. Soc.,* **141,** 563–579, doi:10.1002/qj.2378.

Zhao, Q. Y., and F. H. Carr, 1997: A prognostic cloud scheme for operational NWP models. *Mon. Wea. Rev.,* **125,** 1931–1953, doi:10.1175/1520-0493(1997)125<1931:APCSFO>2.0.CO;2.

Zhu, Z., and E. K. Schneider, 1997: Improvement in stratosphere simulation with a hybrid $\sigma$-$\vartheta$ coordinate GCM. *Quart. J. Roy. Meteor. Soc.,* **123,** 2095–2113, doi:10.1002/qj.49712354315.